

Automated SEM/EDS Analysis for Assessment of Trace Cross-Contamination in 316L Stainless Steel Powders



MARÍA J. BALART, XINJIANG HAO, and CLAIRE L. DAVIS

Following observations of microcracking in two, out of three, Additive manufactured (AM) 316L steel samples, an investigation was undertaken to ascertain the root cause. Welding diagrams, taking into account composition and process parameters, could not generally account for the experimental observations of non-cracked *versus* cracked AM 316L samples. EBSD phase maps in all three AM samples exhibited a fully austenitic microstructure not only in the bulk sample but also near-surface. Analysis of microcracked regions in the AM samples showed the presence of local enrichment of Ni, Cu and P. Automated SEM/EDS analysis on feedstock powder samples prepared for cross-section examination revealed a fine, foreign particulate contaminant, expected to arise from NiCrCuP alloy cross-contamination during atomization, to be completely embedded in a 316L powder particle. This type of contamination would not have been revealed on examination of powder mounted onto a SEM stub, a common approach to assess powder quality. Based on this analysis, it is recommended to consider including automated SEM/EDS analysis on powder cross-sections in any standardization protocol for quality control of powders, to increase the chances of detection and identification of fine cross-contaminants. It is also recommended that atomization of NiCrCuP alloy should no longer precede atomization of 316L alloy.

<https://doi.org/10.1007/s11661-021-06474-4>
© The Author(s) 2021

316L stainless steel is one of the most common grades of austenitic stainless steel and is a versatile material widely being used across many industrial sectors such as offshore, marine, aerospace, nuclear, chemical and bioengineering due to their good combination of mechanical properties and corrosion resistance.^[1] 316L can be reliably additive manufactured (AM).^[2,3] Considerable increase in the complexity of alloys, products and processing routes has resulted from growth in the powder metallurgy sector,^[4–10] in particular the metallic powder supply chain.^[11] This complexity is seen as a source of risks, challenges and opportunities to the broader supply chain for metal

powders, powder processing and manufacturing technologies and increased competition.^[11] A particular challenge is to prevent powder cross-contamination (CC) as this could adversely affect product properties.^[12–17]

Another issue is that solidification cracking can occur during additive manufacturing, as reported by Yu *et al.*^[18] in a recent study on cracking susceptibility of AISI 316L and AISI 304 stainless steels parts produced by laser metal deposition. In that study, diagrams for weld solidification cracking susceptibility of austenitic stainless steels were used for the prediction of cracking susceptibility. It is well-known that 316L stainless steel weld metals are susceptible to solidification cracking due to S and P trace impurity segregation along grain boundaries during the last stages of solidification.^[19] Empirically determined relationships between S + P trace impurity contents, the ratio of Cr equivalent to Ni equivalent and cracking susceptibility have been determined in austenitic stainless steels weld metals, and critical transition boundaries proposed for non-cracking/cracking susceptibility as exemplified in Figure 4 of Reference 18. These findings are summarized in Table I. Furthermore, Si was also found to promote cracking. On the other hand, solidification cracking was not observed at a low S + P + Si level in conjunction with a

MARÍA J. BALART is with the WMG – Advanced Manufacturing and Materials Centre (AMMC), University of Warwick, Coventry CV4 7AL, U.K. and with the WMG – Energy Innovation Centre (EIC), University of Warwick, Coventry CV4 7AL, U.K. Cocontact e-mail: Maria.Balart-Murria@warwick.ac.uk. XINJIANG HAO is with the WMG – Advanced Manufacturing and Materials Centre (AMMC), University of Warwick and also with the Liberty Powder Metals, Materials Processing Institute, Eston Road, Middlesbrough TS6 6US, U.K. CLAIRE L. DAVIS is with the WMG – Advanced Manufacturing and Materials Centre (AMMC), University of Warwick.

Manuscript submitted June 25, 2021; accepted September 27, 2021.

Table I. Experimental Observations and Cracking Susceptibility of AM 316L and 304 Stainless Steels Reported in Ref. [18]

	316L WA (1)	316L GA (2)	316L GA (3)	304 WA (4)	304 GA (5)	304 GA (6)
Si	2.23	0.5	0.53	1.32	0.44	0.34
S + P	0.02	0.041	0.023	0.125	0.035	0.044
S + P + Si	2.25	0.541	0.553	1.445	0.475	0.384
N	0.047	0.09	0.062	—	—	—
AM build	cracking	cracking	non-cracking	cracking	Non-cracking	non-cracking
Regime	experimental observations	non-cracking	non-cracking	cracking	cracking	non-cracking
	suutala diagram, for conventional welding ^[20]	non-cracking	non-cracking	cracking	cracking	non-cracking
	improved Suutala diagram by Pacary, for laser welding ^[21]	non-cracking	non-cracking	cracking	cracking	non-cracking
	improved Suutala diagram by Lundin ^[22]	not susceptible	not susceptible	very susceptible	very susceptible	non-susceptible
	Folkhard ^[23]	non-cracking	non-cracking	cracking	cracking	cracking

Predictions of cracking susceptibility in agreement with experimental observations are both marked with bold.
W/A water atomization, *GA* gas atomization.

low N content for the 316L steel and at a low S + P + Si level for the 304 steel.

A further issue affecting AM product performance is that CC of powder precursors can occur during powder production, handling and additive manufacturing.^[12,13] A general survey was made of contaminants in powder reported in the literature. These are summarized in Table II. Detailed information, where it is reported in the original publication, is organised in columns that include powder type, chemical analysis of elements present entirely or partly in the contaminant, chemical analysis method, contaminant type and form in the powder—discrete particle or embedded in powder where appropriate—, its size, technique used to detect and analyze the contaminant, its origin, other possible sources of contamination as described in the original paper, mechanical property investigated and references.

The most common method for powder assessment, and identification of contamination is to use powders mounted onto a SEM stub^[13] using for example, electrically conductive carbon tape^[26,27,30] or conductive glue.^[25] Contaminants are detected using backscattered electron imaging (BSEI) in conjunction with EDS analysis with automated morphological measurement and EDS data acquisition possible. The morphological and chemical dataset is then classified using a preset or modified classification scheme. The assessment of powder cross-sections prepared for micro-PIXE (proton induced X-ray emission) analysis,^[24] automated inclusion analysis^[30] and grain boundary engineering characterisation,^[31,32] is less commonly used for the characterisation of CC.

It is clear from the examples given in Table II for powder mounted onto a SEM stub that the contaminant particulates were coarse enough, with good atomic contrast to be identified in *quasi*-automated SEM/EDS analysis. There are also examples of where powder cross-sections were analyzed by micro-PIXE, automated inclusion analysis and STEM. The comparative advantage of the automated SEM/EDS analysis is that it is a high throughput technique, as it can combine the latest generation of EDS detectors and algorithms for both speed and accuracy. PIXE is a relatively new technique and, therefore, the accessibility is currently limited.^[24] Sample preparation for STEM analysis required an intermediate layer of 17-4PH powder particles in-between two layers of electroplated Ni. Observations on the CC examples on powder cross-sections are listed in Table II. The three WC - 6 wt pct Co grades analysed by PIXE were granules consisting of aggregates of fine particles 1.7 – 1.8 μm in size, in which Fe was found to be the main impurity in the three grades and was primarily associated to the Co binder phase. Fe impurity levels < 0.3 wt pct in WC-Co alloys are considered normal as Fe arises from recycling of cemented carbide (Fe is sometimes the tough binder phase). The greater Fe impurity levels in the two WC—6 wt pct Co in Table II were attributed to be due to under-loaded milling which could have caused intensifying wear of the stainless steel milling ball as there is a ball-to-powder ratio in ball-milling.^[24] While, the 17-4PH samples analyzed by STEM had some Cr-Mn-Al-Si-containing

Table II. Examples of Cross-Contamination in Powder Materials Reported in the Literature

Powder Type (wt pct)	Chemical Analysis of Elements Present Entirely or Partly in the Contaminant (wt pct)	Chemical Analysis Method	Contaminant Type and Form in the Powder: Discrete Particle or Embedded in Powder	Contaminant Size (μm)	Techniques Sensitive to Detect the Contaminant	Origin of the Contaminant Identified and Other Possible Origins Considered in the Original Paper	Mechanical Properties	References
WC-6Co non-Zn recycled	$0.4941 \pm 0.0314\text{Fe}$	ICP-OES carbon/sulphur analyzer	Fe particles (> 0.3 wt pct)	$5 - 100 \mu\text{m}$ approx. aggregates	ICP-OES and micro-PIXE on powder cross-sections.	Under-loaded milling could have caused intensifying wear of the stainless steel milling ball as there is a ball-to-powder ratio in ball-milling.	—	[24]
WC-6Co Zn recycled	$0.7370 \pm 0.0077\text{Fe}$	ICP-OES carbon/sulphur analyzer	Fe particles (> 0.3 wt pct)	$5 - 50 \mu\text{m}$ approx. aggregates	ICP-OES and micro-PIXE on powder cross-sections.		—	[24]
WC-6Co produced using 70 pct powder from mining grade scrap material	$0.1446 \pm 0.0058\text{Fe}$	ICP-OES carbon/sulphur analyzer	Fe particles (< 0.3 wt pct)	$5 - 40 \mu\text{m}$ approx. aggregates	ICP-OES and micro-PIXE on powder cross-sections.		—	[24]
18Ni-300 maraging steel	$0.6-0.8\text{Ti}-0.05-0.15\text{Al}$	EDS	Discrete Ti-Al oxide powder particles (absence of Fe, Co, Mo and Ni)	$\sim 30 \mu\text{m}$	BSE imaging and EDS on powder mounted onto a SEM stub. Contaminant not detected by ICP-OES.	CC in the AM equipment. Also observed "black powder" (partially melted, oxidized powder collected in the build chamber by filtering). Insufficient mixing in the furnace before atomization.	Decreased fatigue limit. Similar tensile properties tested with and without the contaminant.	[25]

Table II. continued

Powder Type (wt pct)	Chemical Analysis of Elements Present Entirely or Partly in the Contaminant (wt pct)	Chemical Analysis Method	Contaminant Type and Form in the Powder: Discrete Particle or Embedded in Powder	Contaminant Size (μm)	Techniques Sensitive to Detect the Contaminant	Origin of the Contaminant Identified and Other Possible Origins Considered in the Original Paper	Mechanical Properties	References
Ti-6Al-4V alloy	< 0.005W	CGHE (H, O, N) combustion (C) flame AAS (Fe) ICP-OES (Al, V, W, Ti)	Discrete W powder particles	0.03 pct - 0.04 pct by volume. 27 - 140 μm	X-ray CT BSE imaging and EDS on powder mounted onto a SEM stub. Contaminant not detected by ICP-OES	CC in the AM equipment. Also observed W particles entrained from erosion of the tungsten electrode used in the plasma rotating electrode process	A decrease in elongation values; and significant scatter and lower values in both the yield strength and ultimate tensile strength in the build direction.	[26]
Maraging steel	0.9 \pm 0.1Ti-0.02 \pm 0.01Al	EDS	none		BSE imaging and EDS on powder mounted onto a SEM stub.	CC	—	[27]
	1.5 \pm 0.2Ti-0.05 \pm 0.01Al		0.5 wt pct discrete Ti-6Al-4V powder particles	2.0 \pm 0.2			—	[27]
	4.0 \pm 0.1Ti-0.6 \pm 0.3Al		1 wt pct discrete Ti-6Al-4V powder particles	3.6 \pm 0.3			—	[27]
	6.0 \pm 1Ti-0.7 \pm 0.2Al		2.5 wt pct discrete Ti-6Al-4V powder particles	9.7 \pm 0.6			—	[27]

Table II. continued

Powder Type (wt pct)	Chemical Analysis of Elements Present Entirely or Partly in the Contaminant (wt pct)	Chemical Analysis Method	Contaminant Type and Form in the Powder: Discrete Particle or Embedded in Powder	Contaminant Size (μm)	Techniques Sensitive to Detect the Contaminant	Origin of the Contaminant Identified and Other Possible Origins Considered in the Original Paper	Mechanical Properties	References
Ti-6Al-4V alloy	n.d.Fe	EDS	none		BSE imaging and EDS on powder mounted onto a SEM stub.	CC	—	[27]
	n.d.Fe		0.5 wt pct discrete powder particles from maraging steel	1.1 ± 0.4			—	[27]
	$0.8 \pm 0.1\text{Fe}$		1 wt pct discrete powder particles from maraging steel	2.0 ± 0.2			—	[27]
	$1.3 \pm 0.1\text{Fe}$		2.5 wt pct discrete powder particles from maraging steel	5.2 ± 0.2			—	[27]
IN718 alloy	0.480Al		Discrete Al-rich powder particles	$\sim 30 \mu\text{m}$	BSE imaging and EDS on powder cross-sections and powder mounted onto a SEM stub. Contaminant not detected by ICP-OES	CC unknown origin	—	[28]

Table II. continued

Powder Type (wt pct)	Chemical Analysis of Elements Present Entirely or Partly in the Contaminant (wt pct)	Chemical Analysis Method	Contaminant Type and Form in the Powder: Discrete Particle or Embedded in Powder	Contaminant Size (μm)	Techniques Sensitive to Detect the Contaminant	Origin of the Contaminant Identified and Other Possible Origins Considered in the Original Paper	Mechanical Properties	References
17-4PH stainless steel	16.7Cr-0.48Mn-0.67Si (nominal composition)	Cr-Mn-Al-Si containing oxide particles embedded in the powder	1.5 μm	STEM on powder cross-sections.	Oxides entrained in the melt from erosion of crucible or nozzle liners during gas atomisation. Also observed slag entrained in the melt during gas atomisation.	—	[29]	

CGHE Carrier gas hot extraction, ICP OES inductively coupled plasma optical emission spectrometry, AAS flame atomic absorption spectroscopy, n.d. not detected.
 Combustion: IR analysis of the combustion gas.
 — not determined or reported in the original publication.

oxide particles with one example reported to be 1.5 μm in size, completely embedded and close to the center of the powder particle of $\sim 10 \mu\text{m}$ in cross-section size (see Figure 8 of Reference 29).

Here, we report observations of microcracks found during SEM examination of two AM 316L samples, which were built using two different compositional powders from the same commercial supplier. Conversely, no microcracks were found in another AM 316L sample which was built using another powder from a different commercial supplier and with the same AM machine parameters. Following failure of the two 316L steels during AM building, an investigation was undertaken to ascertain the root cause. To this end, the cracking susceptibility has been assessed using the methodology described by Yu *et al.*^[18] based on the original works by Suutala and Moiso,^[20] Pacary *et al.*,^[21] Lundin *et al.*^[22] and Folkhard^[23] together with the residual S + P, Si and N levels, as highlighted in their work.^[18] Automated SEM/EDS analysis has been utilized for assessment of trace levels of CC in 316L powder on cross-sections.

Three different types of 316L stainless steel powders ($< 150 \mu\text{m}$) produced by air-melted gas atomization (AMGA) were provided by Liberty Powder Metals from two suppliers (A and B). The 316L powder from supplier A was sieved to 15 to 45 μm and the other two 316L powder samples from supplier B were sieved to 20 to 64 μm . All three powders were AM using SLM with a Renishaw AM 250 with the same standard parameters from the machine manufacturer Renishaw. 10 mm \times 10 mm \times 55 mm AM samples were built in the longitudinal direction.

The chemical composition of the 316L steel powders and the corresponding AM samples investigated as well as the minimum and maximum values as per steel specification ASTM A240^[33] are given in Table III. The C, S, N and O contents of the samples were analyzed by LECOTM. The other elements were analyzed by inductively coupled plasma optical emission spectrometry (ICP-OES).

1 g of each powder composition was cold mounted in epoxy resin, ground and polished to a 0.05 μm non-crystallizing SiO₂ polishing suspension finish. Cross-sections parallel to the build direction were mounted in conductive Bakelite and were also ground and polished to a 0.05 μm non-crystallizing SiO₂ polishing suspension finish.

First, secondary electron imaging and EDS were carried out on AM samples using a Zeiss Sigma FEG-SEM operating at 10 kV. Elemental analyses and EDAX mappings were processed using the AztecFeature OI software that integrates EDS analysis software with an XMax 50 SDD (Silicon Drift Detector).

Second, automated SEM in BSEI mode in conjunction with EDS analysis were carried out on polished powders using a Versa 3D dual beam SEM operating at 10 kV. Elemental analyses were processed using the AztecFeature OI software feature that integrates EDS analysis software with an XMax 80 SDD detector. Powder samples required cold mounting and Au sputtering in an Agar auto sputter coater, using a setting of

Table III. Chemical Composition (Wt Pct) of the Investigated 316L Steels

ASTM	A240 ^[33]	B	Co	Cr	Cu	Mn	Mo	Ni	P	Si	V	W
				16.0-18.0	—	2.00 max.	2.00- 3.00	10.0- 14.0	0.045 max.	0.75 max.		
<i>Supplier A</i>												
Powder A1	15 – 45 μm	< 0.02	0.04	16.67	0.07	0.53	2.32	12.49	0.017	0.6	0.04	< 0.02
<i>Supplier B</i>												
Powder B1	20 – 64 μm	< 0.02	0.43	16.64	0.48	1.22	2.06	10.66	0.037	0.45	0.07	0.11
B2	20 – 64 μm	< 0.02	0.02	16.72	0.06	0.55	2.46	12.51	0.013	0.43	0.02	< 0.02
Uncracked AM 316L sample A1		< 0.02	0.15	16.55	0.11	0.62	2.43	12.18	0.02	0.73	0.025	0.02
Cracked AM 316L sample B1		< 0.02	0.43	15.73	0.45	1.16	2.08	10.58	0.045	0.46	0.07	0.12
Cracked AM 316L sample B2		< 0.02	0.02	16.57	0.06	0.88	2.56	11.49	0.015	0.34	0.02	< 0.02
ASTM	A240 ^[33]	Sn	Ta	Al	Ti	Nb	C	S	N	O	Fe	
							0.030 max.	0.03 max.	0.10 max.			bal.
<i>Supplier A</i>												
Powder A1	15 – 45 μm	< 0.02	< 0.02		< 0.02	< 0.02	0.0241	0.0069	0.0887	0.0627		bal.
<i>Supplier B</i>												
Powder B1	20 – 64 μm	< 0.02	< 0.02	< 0.05	< 0.02	< 0.02	0.0085	0.0173	0.0271	0.0642		bal.
B2	20 – 64 μm	< 0.02	< 0.02	< 0.05	< 0.02	< 0.02	0.0164	0.0046	0.0581	0.0467		bal.
Uncracked AM 316L sample A1		< 0.02	< 0.02	< 0.05	< 0.02	< 0.02	0.0300	0.0056	0.0998	0.0567		bal.
Cracked AM 316L sample B1		< 0.02	< 0.02	< 0.05	< 0.02	< 0.02	0.0147	0.0142	0.0247	0.0636		bal.
Cracked AM 316L sample B2		< 0.02	< 0.02	< 0.05	< 0.02	< 0.02	0.0275	0.0041	0.0593	0.0459		bal.

— There is no requirement, and analysis for the element need not be determined or reported.

40 mA, for 30 sec. AztecFeature OI software was used to identify foreign particles in the powder samples. EBSD maps were collected from AM samples at 20 kV accelerating voltage and 0.5 μm step size. Phase maps were also processed using Aztec OI software.

BSEI and EDAX mapping of elements identified Ni-Cu-P-rich regions near the microcracks in the bulk of the two AM 316L samples from the second powder supplier. Two examples are shown in Figures 1 and 2. The significance of this observation will be discussed below. In contrast, the AM 316L sample from the first powder supplier did not crack, Figure 3. Experimental observations and cracking susceptibility predictions according to the aforementioned study by Yu *et al.*^[18] together with the residual S + P, Si and N levels are given in Table IV and are plotted in Figure 4. Yu *et al.*'s results^[18] are also represented for comparative purposes. EBSD phase maps in all three AM samples exhibited a fully austenitic microstructure not only in the bulk sample but also near-surface, as exemplified in Figures 1(b) and (c), 2(c) and (d) and 3(a) through (c).

Failure of the two 316L steels during AM would not be initially expected given the fact that 316L can consistently be AM,^[2,3] and that the values of S + P + Si and N levels (in wt pct) for the cracked AM 316L

sample B2 are lower than those for the uncracked AM 316L sample, but the S + P level is higher, Table IV. The cracking susceptibility predictions, Table IV and Figure 4, from the abovementioned welding diagrams cannot generally account for the experimental observations of non-cracked *versus* cracked AM 316L samples.

The values of S + P, S + P + Si and N levels (in wt pct) for the uncracked AM 316L sample of the present investigation are 0.024 wt pct, 0.624 wt pct and 0.089 wt pct, respectively compared with the values given in Reference 18: 0.023 wt pct, 0.553 wt pct and 0.062 wt pct, for the uncracked AM 316L sample; and 0.041 wt pct, 0.541 wt pct and 0.09 wt pct, for the cracked AM 316L sample. This suggests the requirement of low S + P impurity levels (< 0.024 wt pct) at the high N contents of 0.062 wt pct and 0.089 wt pct for uncracking.

An automated BSEI of the area of analysis for the initial 316L powder B1 (< 150 μm) is shown in Figure 5(a). 6043 fields of 59 x 85.8 x 10⁻⁶ mm² each and an area of resin of 16.2 mm² were analysed corresponding to a scanned area of 14.4 mm² and > 10,000 particles. BS ISO 13322-1:2014^[38] and NIST^[39] recommended to measure around 10,000 particles for statistical robustness as determined by the relative standard deviation for

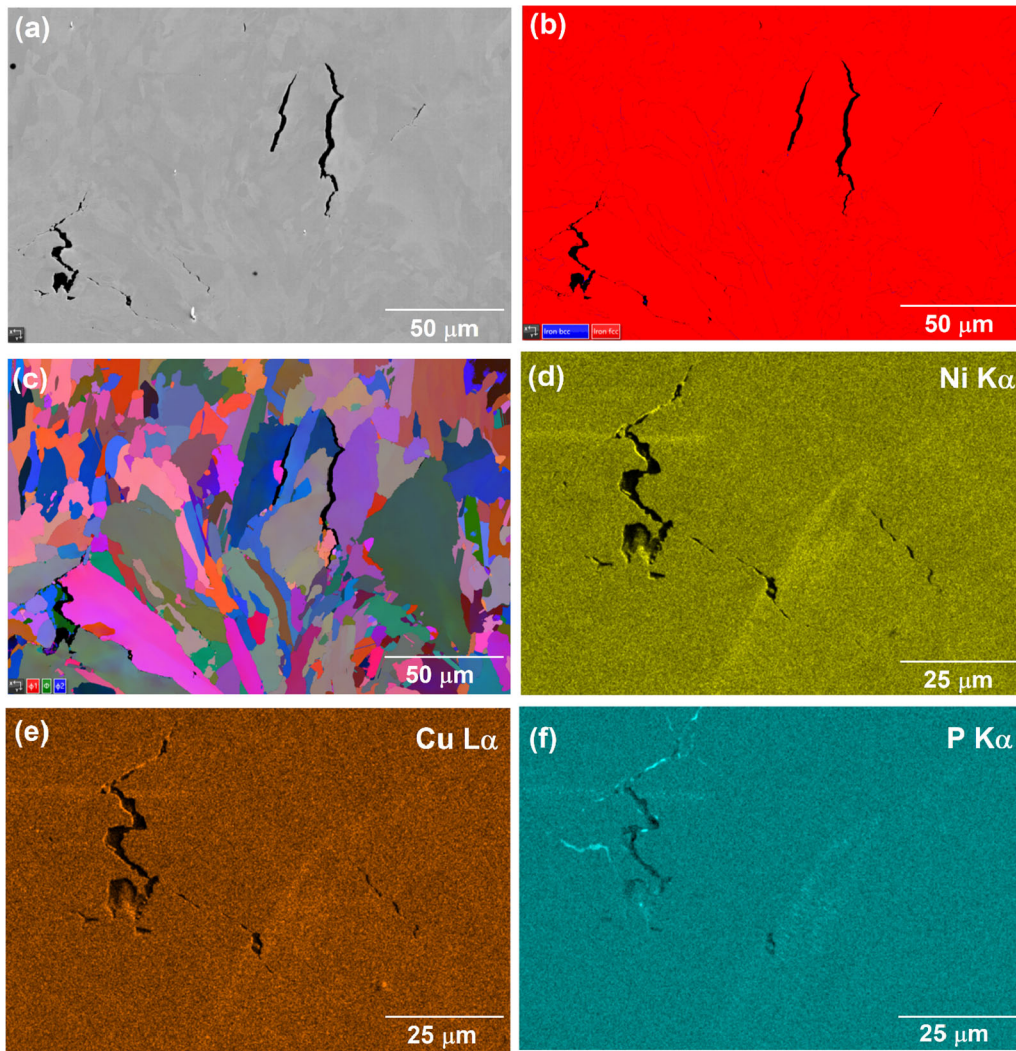


Fig. 1—Microcracks in the AM 316L sample from powder B1 (a) BSE micrograph, (b) phase map, (c) EBSD micrograph, and mapping of elements (d) Ni, (e) Cu and (f) P. Cross-sections taken along the build direction from top to bottom of the page.

morphological shape descriptors such as particle size and shape factors. It is expected that some particles could be contaminants.

From Figure 5(a), a fine, foreign particulate contaminant, completely embedded in a 316L powder particle was sampled as shown in Figures 5(b) through (d). This is indicative of CC during atomization. Its EDS analysis is given in Table V. Following our analysis and communication with the supplier, it was confirmed that the observed foreign particulate originated from CC from previous production material—a low-melting NiCrCuP alloy powder—melting temperature 1173 K (900 °C) approx. compared with 1673 K (1400 °C) for 316L steel—. The major differences between the 1.5 μm

sized inclusion shown in Figure 8 of Reference 29 and the inclusion shown in Figures 5(b) through (d) are that the melting point of the oxide contaminant particulate is higher than the surrounding steel matrix, as opposed to the low-melting NiCrCuP alloy contaminant of Figure 5, and while in the former case the contaminant is located close to the centre of the powder particle, in the latter case the contaminant is located near-surface. Both are fine, foreign particulate contaminants, though. The high stability and high melting temperatures of refractory oxide contaminants mean that these could have been engulfed by droplets of molten steel during solidification. By contrast, in the present investigation, the opposite trend has been observed. It is possible that

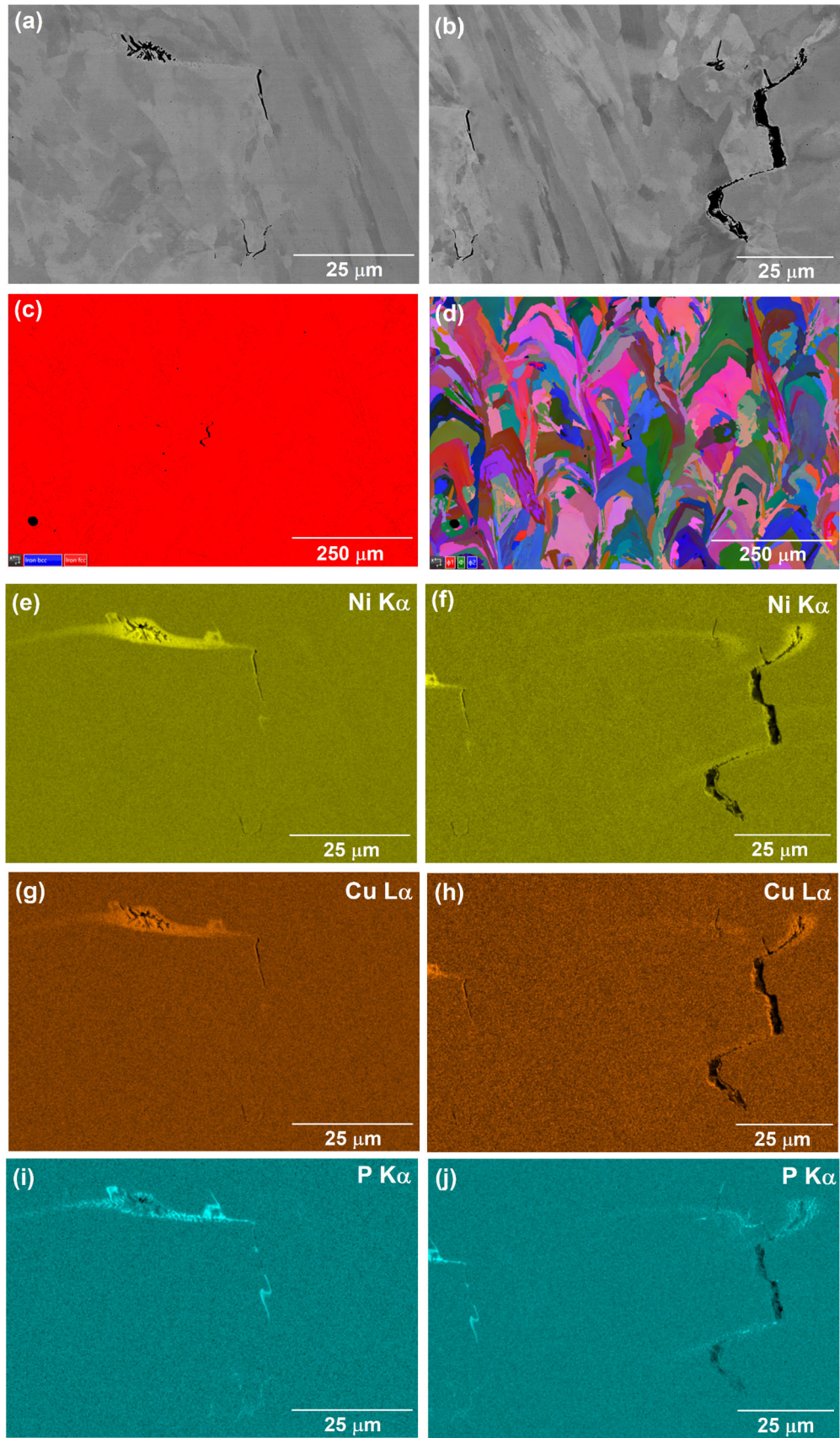


Fig. 2—Microcracks in the AM 316L sample from powder B2 (*a*) and (*b*) BSE micrographs, (*c*) phase map, (*d*) EBSD micrograph and mapping of elements (*e*) and (*f*) Ni, (*g*) and (*h*) Cu and (*i*) and (*j*) P. Cross-sections taken along the build direction from top to bottom of the page.

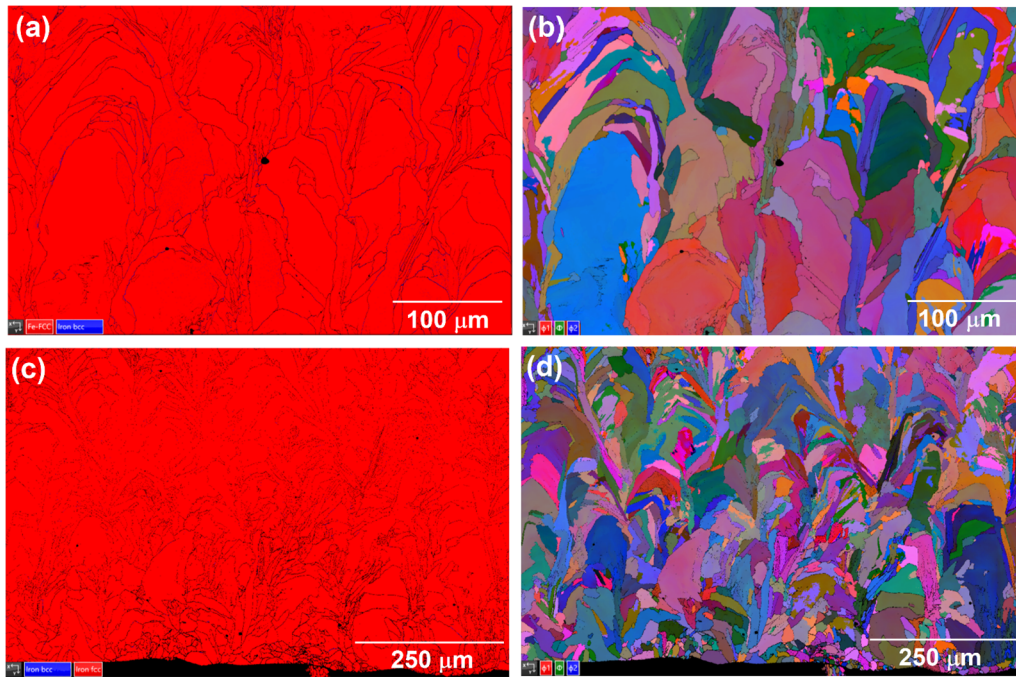


Fig. 3—AM 316L sample from powder A1 (a) and (b) bulk sample and (c) and (d) near-surface: (a) and (c) phase maps and (b) and (d) EBSD micrographs. Cross-sections taken along the build direction from top to bottom of the page.

rapid impingement and engulfment of droplets during atomization could have caused low-melting point contaminants to be embedded near-surface in the higher melting point steel matrix

It is interesting to note that the CC particle is fully embedded in the 316L powder particle, and therefore would not be observable unless powder cross-sections are analyzed. It also suggests that the probability of detecting the contamination may be low (typically have low levels of CC coupled with a sectioning effect). It would appear that in this case there was significant CC as it resulted in a significant area of locally enriched composition, Figures 1 and 2, that caused microcracking. From microcracking observations in the present investigation, atomization of NiCrCuP alloy should no longer precede atomization of 316L alloy as CC is causing cracking susceptibility.

Our communication with the supplier has helped to resolve the root cause of the CC issue during atomization on this occasion, as it has been possible to track the material that preceded atomization of the 316L steels of the present investigation. The low-melting NiCrCuP

alloy contaminant was found to be wholly embedded in the 316L particle, indicating that CC occurred in the melting vessel / atomization nozzle. It is clear that by solely cleaning the collection chamber, the problem is not solved. An example from the literature in which CC occurred in the melting vessel, but due to oxides entrained in the melt from erosion of crucible or nozzle liners during gas atomisation of the 17-4PH steel, is given in Table II. Likewise, the oxide contaminant was found to be wholly embedded in the 17-4PH powder particle, as outlined above. Sun *et al.*^[29] highlighted that advanced atomization techniques prevent the melt being in contact with potential contamination sources. These are, however, more expensive techniques and infrequently used for replacement of standard atomization. On the grounds that it is challenging the detection of contaminants in the feedstock powder and when CC occurs in the AM machine, Brandão *et al.*^[26] recommended using one AM machine per feedstock powder for critical applications such as aerospace.

In the studies summarized in Table II, the results of the ICP analysis for 18Ni-300 maraging steel,^[25]

Table IV. Experimental Observations and Cracking Susceptibility of the Investigated 316L Steels

		[18]	A1, 15 – 45 μm	B1, 20 – 64 μm	B2, 20 – 64 μm
	DeLong ^[34]				
Cr _{eq}	Cr + Mo + 1.5Si + 0.5Nb	19.89	19.38	19.83	
Ni _{eq}	Ni + 0.5Mn + 30C + 30N	16.14	12.34	15.02	
Cr _{eq} /Ni _{eq}		1.23	1.57	1.32	
Phase		A	FA	AF	
	Schaeffler ^[35]				
Cr _{eq}	Cr + Mo + 1.5Si + 0.5Nb	19.89	19.38	19.83	
Ni _{eq}	Ni + 0.5Mn + 30C	13.48	11.53	13.28	
Cr _{eq} /Ni _{eq}		1.48	1.68	1.49	
Phase		FA	FA	FA	
	WRC-1992 (Siewert) ^[36]				
Cr _{eq}	Cr + Mo + 0.7Nb	18.99	18.70	19.18	
Ni _{eq}	Ni + 35C + 20N + 0.25Cu	15.13	11.62	14.26	
Cr _{eq} /Ni _{eq}		1.26	1.61	1.34	
Phase		AF	FA	AF	
	HS (Hammar, Svennson) ^[37]				
Cr _{eq}	Cr + 1.37Mo + 1.5Si + 2 Nb + 3Ti	20.75	20.14	20.74	
Ni _{eq}	Ni + 0.31Mn + 22C + 14.2N + Cu	14.51	12.09	13.93	
Cr _{eq} /Ni _{eq}		1.43	1.67	1.49	
Phase		AF	FA	FA	
Si		0.6	0.45	0.43	
S + P		0.024	0.054	0.018	
S + P + Si		0.624	0.504	0.448	
N		0.089	0.027	0.058	
AM build	Experimental observations	non-cracking	cracking	cracking	
Regime	Folkhard diagram ^[23]	cracking	non-cracking	non-cracking	
calculated from	Improved Suutala diagram	cracking	non-cracking	cracking	
Cr _{eq} /Ni _{eq} HS ^[34]	by Lundin <i>et al.</i> ^[22]				
	Improved Suutala diagram	very susceptible	not susceptible	not susceptible	
	by Pacary <i>et al.</i> for laser welding ^[21]				
WRC ferrite No.	Suutala diagram, for conventional welding ^[20]	non-cracking	cracking	non-cracking	
		5	7	7	

Predictions of cracking susceptibility in agreement with experimental observations are both marked with bold.

Ti-6Al-4V alloy^[26] and IN718 alloy^[28] powders indicated that the elements in the corresponding contaminants, namely Ti-Al oxides, W and Al-rich particles, were present at levels within the specification limits. Whereas ICP analysis in WC-6Co cemented carbides^[24] identified Fe impurities to be in excess of the normal limits < 0.3 wt pct. From the chemical composition analysis in Table III, it may be seen that the contents of Ni and P are within the specification of ASTM A240.

Overall, these results have important implications for the development of standardization tools to increase the chances to detect, identify and track CC for quality control of powders introduced in the supply chain as very small amounts of contamination can be identified in powder cross-sections.

This investigation has been undertaken to ascertain the root cause of microcracking through comparing the results of a non-cracked *versus* two cracked AM 316L samples:

- Welding diagrams, taking into account composition and process parameters, could not generally account for the experimental observations of non-cracked *versus* cracked AM 316L samples. EBSD phase maps in all three AM samples exhibited a fully austenitic microstructure not only in the bulk sample but also near-surface. The uncracked AM 316L sample suggested very low levels of trace impurity elements S+P impurity levels (< 0.024 wt pct) are required at the high N content of 0.09 wt pct.

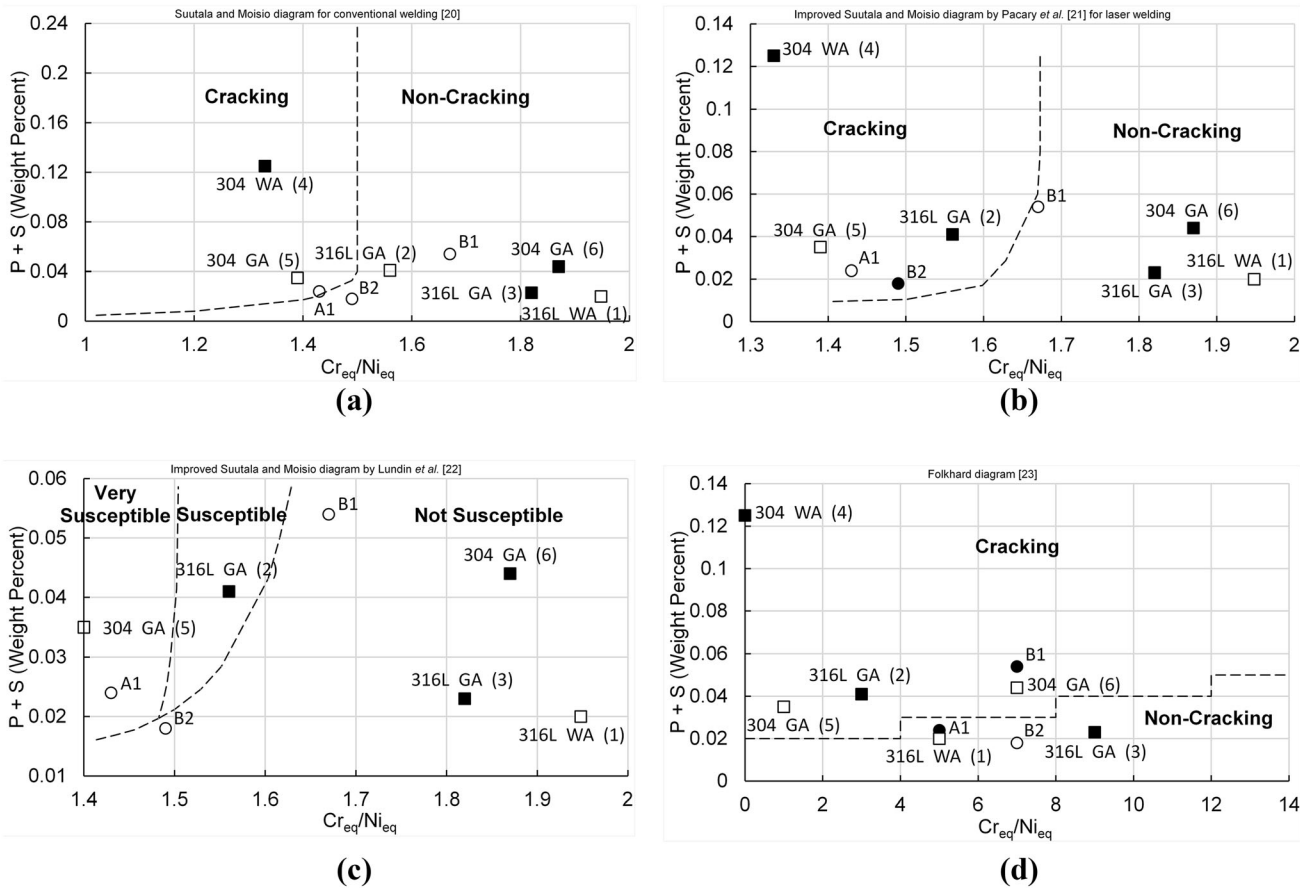


Fig. 4—Experimental observations and cracking susceptibility predictions from Tables I and IV in line with the work of Yu *et al.*^[18] (a) Suutala and Moiso diagram for conventional welding,^[20] (b) improved Suutala and Moiso diagram by Pacary *et al.*^[21] for laser welding, (c) improved Suutala and Moiso diagram by Lundin *et al.*^[22] for laser welding and (d) Folkhard diagram.^[23] Predictions of cracking susceptibility in agreement with experimental observations are marked with filled symbols, otherwise with unfilled symbols: squares symbols represent data adapted from Ref. [18] and circle symbols represent experimental observations of the present investigation. Reprinted with permission from Ref. [18] copyright 2013, Elsevier, <https://doi.org/10.1016/j.matdes.2012.08.078>.

Cracking was observed to be associated with a local enrichment in Ni, Cu and P levels.

- Automated SEM/EDS analysis on powder cross-sections sampled a fine, foreign particulate contaminant from NiCrCuP alloy to be embedded in a 316L powder particle, which would not have been revealed by analysis of powder particles mounted onto a SEM stub. The NiCrCuP originated as CC from the previous atomization batch, and it is suspected that it resulted in the local composition enrichment which was associated with cracking. Based on this analysis, it is recommended to consider including automated SEM/EDS analysis on powder cross-sections in any standardization protocol for quality control of

powders, to increase the chances of detection and identification of fine cross-contaminants. It is also recommended that atomization of NiCrCuP alloy should no longer precede atomization of 316L alloy.

The financial support of Liberty Powder Metals is gratefully acknowledged. This work was carried out as part of UK government's Advanced Manufacturing Supply Chain Initiative (AMSCI)—CASCADE project: Creating an advance manufacturing supply chain for net shape and AM parts which address the demands of end-users.

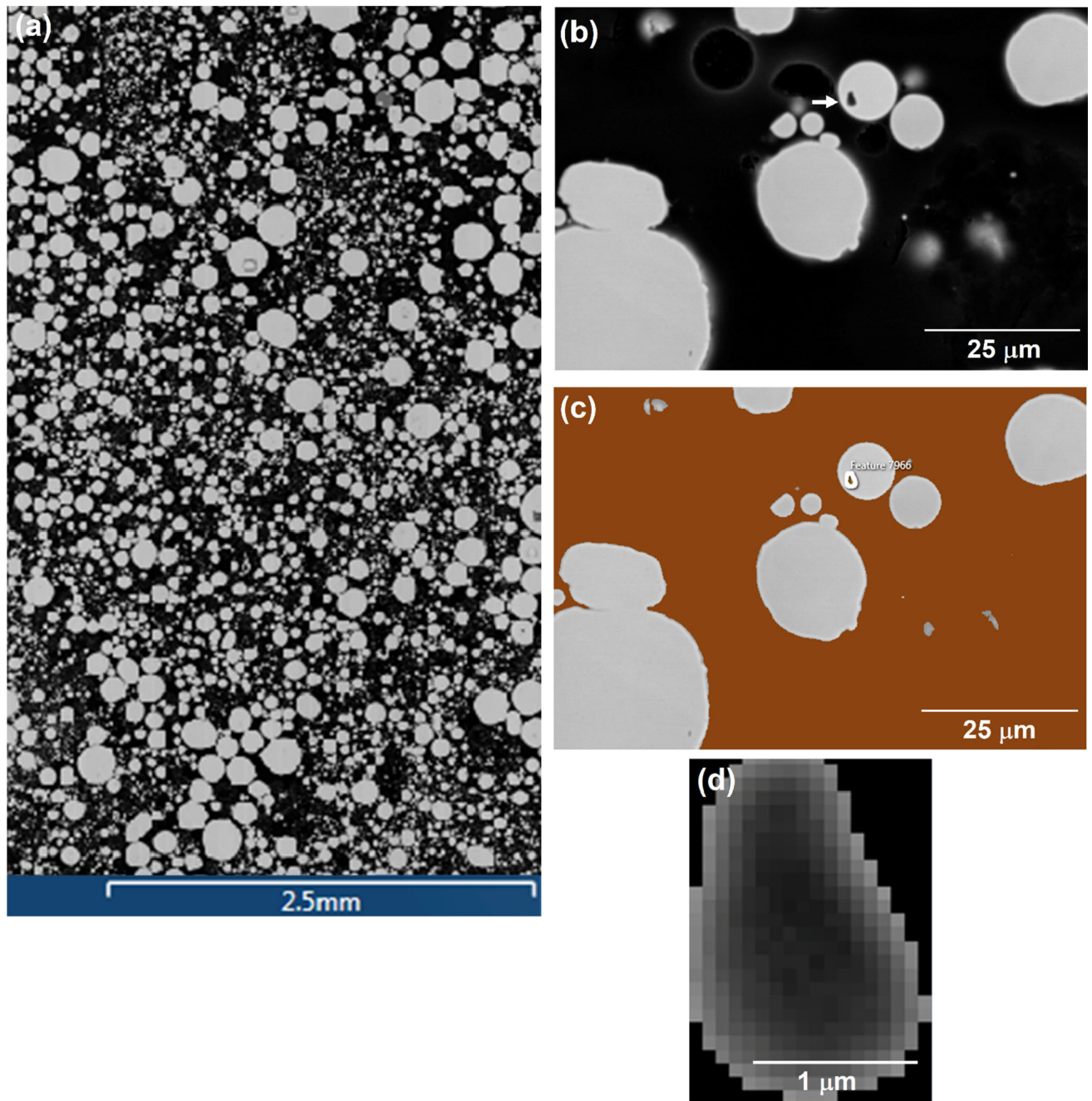


Fig. 5—(a) BSE macrograph for the 316L < 150 μm powder B1 showing the area of analysis: $59 \times 85.8 \times 10^{-6} \text{ mm}^2$ size of field, 6043 number of fields, 16.2 mm^2 area of resin and 14.4 mm^2 area scanned. A fine, foreign particulate contaminant (arrowed) completely embedded in a 316L powder particle (b) BSEI, (c) Imaging from a single grey threshold for detecting the contaminant and (d) BSEI of particulate contaminant in (b).

Table V. EDS Analysis (Wt Pct) From the NiCrCuP Alloy Particulate Contaminant in Fig. 5(d)

Ni	C	Cr	Cu	O	Si	P	Fe
52.6 ± 1.1	11.2 ± 1.5	10.0 ± 0.3	7.2 ± 0.5	5.7 ± 0.6	5.7 ± 0.2	4.5 ± 0.3	3.0 ± 0.2

The authors declare that they have no known competing financial interests or personal relationships that could have appeared to influence the work reported in this paper.

OPEN ACCESS

This article is licensed under a Creative Commons Attribution 4.0 International License, which permits use, sharing, adaptation, distribution and reproduction in any medium or format, as long as you give appropriate credit to the original author(s) and the source, provide a link to the Creative Commons licence, and indicate if changes were made. The images or other third party material in this article are included in the article's Creative Commons licence, unless indicated otherwise in a credit line to the material. If material is not included in the article's Creative Commons licence and your intended use is not permitted by statutory regulation or exceeds the permitted use, you will need to obtain permission directly from the copyright holder. To view a copy of this licence, visit <http://creativecommons.org/licenses/by/4.0/>.

REFERENCES

1. J.R. Davis, ed., ASM Speciality Handbook. Stainless Steels, 2nd ed., ASM International, Materials Park, OH, 1994.
2. M.J. Heiden, L.A. Deibler, J.M. Rodelas, J.R. Koepke, D.J. Tung, D.J. Saiz, and B.H. Jared: *Addit. Manuf.*, 2019, vol. 25, pp. 84–103, <https://doi.org/10.1016/j.addma.2018.10.019>.
3. A.S. Wu, D.W. Brown, M. Kumar, G.F. Gallegos, and W.E. King: *Metall. Mater. Trans. A*, 2014, vol. 45A (13), pp. 6260–70, <https://doi.org/10.1007/s11661-014-2549-x>.
4. U. Engström and E. Schneider: in *World Congress on Powder Metallurgy, Proceedings of World PM2018, Beijing, China*, 16-20 September 2018, pp. 43-52.
5. V. Polard and B. Blitz: in *World Congress on Powder Metallurgy, Proceedings of World PM2018, Beijing, China*, 16-20 September 2018, pp. 1152-55.
6. R. Goto: in *World Congress on Powder Metallurgy, Proceedings of World PM2018, Beijing, China*, 16-20 September 2018, pp. 1979-82.
7. P. Gundermann: in *Euro PM2018 Plenary presentation, Bilbao, Spain*, 14-18 October 2018. <https://www.europm2018.com/onsite-content-access>. Accessed 24 June 2021.
8. P. Bajaj, A. Hariharan, A. Kini, P. Kürnsteiner, D. Raabe, and EA. Jäggle: *Mater. Sci. Eng. A*, 2020, vol. 772, art. no. 138633 <https://doi.org/10.1016/j.msea.2019.138633>.
9. N. Li, S. Huang, G. Zhang, R. Qin, W. Liu, H. Xiong, G. Shi, and J. Blackburn: *J. Mater. Sci. Technol.*, 2019, vol. 35 (2), pp. 242–69, <https://doi.org/10.1016/j.jmst.2018.09.002>.
10. H. Fayazfar, M. Salarian, A. Rogalsky, D. Sarker, P. Russo, V. Paserin, and E. Toyserkani: *Mater. Des.*, 2018, vol. 144, pp. 98–128, <https://doi.org/10.1016/j.matdes.2018.02.018>.
11. J. Dawes, R. Bowerman, and R. Trepleton: *Johnson Matthey Technol. Rev.*, 2015, vol. 59 (3), pp. 243–56, <https://doi.org/10.1595/205651315X688686>.
12. E. Santecchia, P. Mengucci, A. Gatto, E. Bassoli, L. Denti, F. Bondioli, and G. Barucca: in *Euro PM2018 Proceedings, Bilbao, Spain*, 14-18 October 2018.
13. C. Blackwell, S. Hall, J. Dawes, and N. Brierley: in *Euro PM2018 Proceedings, Bilbao, Spain*, 14-18 October 2018.

14. B. Mooney and K.I. Kourousis, *Metals*, 2020, vol. 10, 1273. <https://doi.org/10.3390/met10091273>.
15. M. Montazeri, R. Yavari, P. Rao, and P. Boulware: *J. Manuf. Sci. Eng.*, 2018, vol. 140(11), 111001. <https://doi.org/10.1115/1.4040543>.
16. E. Santecchia, P. Mengucci, A. Gatto, E. Bassoli, L. Denti, B. Gheorghiu, and G. Barucca: in *Euro PM2019 Proceedings, Maastricht, The Netherlands*, 13-16 October 2019.
17. M. Horn, L. Langer, M. Schafnitzel, S. Dietrich, G. Schlick, C. Seidel, and G. Reinhart: *Procedia CIRP*, 2020, Vol. 94, pp. 167-72. In 11th CIRP Conference on Photonic Technologies, LANE 2020; Virtual, Online, 7-10 September 2020.
18. J. Yu, M. Rombouts, and G. Maes: *Mater. Des.*, 2013, vol. 45, pp. 228–35, <https://doi.org/10.1016/j.matdes.2012.08.078>.
19. J.A. Brooks and A.W. Thompson: *Int. Mater. Rev.*, 1991, vol. 36 (1), pp. 16–24, <https://doi.org/10.1179/imr.1991.36.1.16>.
20. N. Suutala and T. Moiso: *Solidification Technology in the Foundry and Casthouse*, The Metals Society, London, 1980.
21. G. Pacary, M. Moline, and J.C. Lippold: EWI research brief no. B9008, 1990, Edison Welding Institute.
22. C.D. Lundin, C.H. Lee, and C.Y.P. Qiao: Group sponsored study-weldability and hot ductility behavior of nuclear grade austenitic stainless steels, Final report, Knoxville: Univ. of Tennessee, 1988.
23. E. Folkhard: *Welding metallurgy of stainless steels*, Springer Verlag, New York, 1988.
24. C.S. Freemantle, N. Sacks, M. Topic, and C.A. Pineda-Vargas: *Int. J. Refract. Met. Hard Mater.*, 2014, vol. 44, pp. 94–102, <https://doi.org/10.1016/j.ijrmhm.2014.01.019>.
25. A. Gatto, E. Bassoli, and L. Denti: *Addit. Manuf.*, 2018, vol. 24, pp. 13–19, <https://doi.org/10.1016/j.addma.2018.09.004>.
26. A.D. Brandão, R. Gerard, J. Gumpinger, S. Beretta, A. Makaya, L. Pambaguian, and T. Ghidini: *Materials*, 2017, vol. 10, 522, <https://doi.org/10.3390/ma10050522>.
27. E. Santecchia, P. Mengucci, A. Gatto, E. Bassoli, S. Defanti, and G. Barucca: *Materials*, 2019, vol. 12, 2342; <https://doi.org/10.3390/ma12152342>.
28. M.J. Balart, X. Hao, S. Marks, G.D. West, and C.L. Davis: in *Euro PM2019 Proceedings, Maastricht, The Netherlands*, 13-16 October 2019.
29. Y. Sun, R.J. Hebert, and M. Aindow: *Mater. Des.*, 2017, vol. 140, pp. 153–62, <https://doi.org/10.1016/j.matdes.2017.11.063>.
30. M.J. Balart, X. Hao, S. Marks, G.D. West, M. Walker, and C.L. Davis: *Metall. Mater. Trans. A*, 2020, vol. 51A (12), pp. 6439–60, <https://doi.org/10.1007/s11661-020-06010-w>.
31. S. Irukuvarghula, H. Hassanin, C. Cayron, MM. Attallah, D. Stewart, and M. Preuss: *Acta Mater.*, 2017, vol. 133, pp. 269–81, <https://doi.org/10.1016/j.actamat.2017.04.068>.
32. M.J. Balart, H.G.C. Hamilton, X. Hao, M. Strangwood, and C.L. Davis: in *Euro PM2018 Proceedings, Bilbao, Spain*, 14-18 October 2018.
33. ASTM A240 / A240M–20a: *Standard Specification for Chromium and Chromium-Nickel Stainless Steel Plate, Sheet, and Strip for Pressure Vessels and for General Applications*, ASTM International, West Conshohocken, PA, 2020, www.astm.org.
34. W.T. DeLong: *Weld. J. Res. Suppl.*, 1974, vol. 53, pp. s273–86.
35. A.L. Schaeffler: *Met. Prog.*, 1949, vol. 56 (11), pp. 680–88.
36. D.J. Kotecki and T.A. Siewert: *Weld J.*, 1992, vol. 71 (5), pp. 171–78.
37. O. Hammer and U. Svensson: *Solidification and Casting of Metals*, The Metals Society, London, 1979, pp. 401–10.
38. BS ISO 13322-1:2014: *Particle size analysis - Image analysis methods – Part 1: Static image analysis methods*, 2014, www.iso.org.
39. A. Jillavenkatesa, S.J. Dapkunas, and L.-S. H. Lum: *NIST Recommended Practical Guide Special Publication 960-1, Particle Size Characterization*, January 2001.

Publisher's Note Springer Nature remains neutral with regard to jurisdictional claims in published maps and institutional affiliations.